RSC Sustainability

ROYAL SOCIETY OF CHEMISTRY

PAPER

View Article Online
View Journal | View Issue

Cite this: *RSC Sustainability*, 2025, **3**, 3184

Screen printability assessment of water-based composite electrodes for lithium-ion batteries†

Nora Chelfouh,[a] Ngoc Duc Trinh,[b] Chloé Bois,[b] Audrey Laventure *[a] and Mickaël Dollé *[a]

Screen printing is a processing technique that presents significant advantages as it is versatile, low-cost and generates minimal amounts of waste. These features make this technique of interest for use in the production of battery electrodes. However, it is important to understand that changing how the composite electrode is manufactured can impact its microstructure and thus its properties. This study highlights the importance of assessing whether a material presents the appropriate properties to be processed *via* a specific printing technique (screen printing *vs.* rod coating) to reach the targeted properties of the composite electrode. More specifically, an evaluation of the printability of water-based composite electrode inks that were formulated with a bio-based polymeric binder (carboxymethyl cellulose) is presented in the context of flat bed screen printing and conventional rod coating. An assessment of the wettability of the ink and its rheological characterization enable the suspension formulation to be adapted to the requirements of each processing technique while ensuring the reproducibility of the suspension formulations for both manufacturing processes. This study demonstrates that screen printing, which allows for significant flexibility and design freedom, can be used to produce composite electrodes as their electrochemical characterization suggests that their performance is similar to that of electrodes prepared using rod coating techniques.

Received 24th March 2025
Accepted 28th May 2025

DOI: 10.1039/d5su00211g

rsc.li/rscsus

Sustainability spotlight

From small sensors to advanced wearable devices, the Internet of Things (IoT) plays a role in our daily lives, particularly within the medical and food packaging industries. Numerous studies have demonstrated the effectiveness of these systems; however, the methods by which these devices are powered remain insufficiently explored. Lithium-ion battery technology is regarded as the default option for IoT applications and has been a focal point of discussion for several years. This technology is recognized for its high energy density, offering enhanced autonomy while maintaining a lighter weight—qualities that are particularly beneficial for portable devices. Nevertheless, further development and manufacturing efforts are necessary to adapt these batteries for sustainable use in small IoT devices, such as flexible sensors. Our focus here is to develop an efficient protocol to assess the printability of water-based ink for composite positive electrodes in lithium-ion batteries. This study promotes a new approach to the processability of composite electrodes using screen printing technologies. Water-based inks with biobased polymer binders for composite electrodes have not yet been widely developed for manufacturing positive electrodes. This work demonstrates the feasibility of such an approach and benchmarks the screen printing methodology with the more conventional rod-coating technique, leading to a new printed composite electrode design that could be beneficial for their implementation in IoT devices. Thus, our research highlights the importance of the following UN Sustainable Development Goals: affordable and clean energy (SDG 7), industry, innovation, and infrastructure (SDG 9), and climate action (SDG 13).

1. Introduction

Lithium-ion batteries, which have been commercialized for over 30 years, are one of the major systems used for energy storage.[1–3] Recent research focuses on enhancing the energy density or power of these devices as demand is expected to increase due to pressure to meet existing goals for sustainable development.[4] To this end, new manufacturing processes for Li-ion batteries are major topics that need to be addressed to reduce the energy costs associated with the increasing demand for this technology.[5–7]

The realm of battery manufacturing entails the meticulous arrangement of numerous composite electrodes within a specific casing. These composite electrodes are generally prepared as suspensions called slurries that contain a mixture of an active material, carbon additives and a fluorinated polymer binder. This mixture is spread on a metallic current collector and is dried and calendered before being integrated

[a]*Département de Chimie, Université de Montréal, 1375 Avenue Thérèse-Lavoie-Roux, P.O. Box 6128, Stn Downtown, Montréal, QC H2V 0B3, Canada. E-mail: mickael.dolle@umontreal.ca; audrey.laventure@umontreal.ca; Tel: +1-514-343-7054, +1-514-343-6282*

[b]*Institut des Communications Graphiques et de l'imprimabilité, 999 Avenue Émile-Journault, Montréal, QC H2M 2E2, Canada*

† Electronic supplementary information (ESI) available: Experimental results regarding ink formulation, contact angle measurements, rheology, mercury intrusion porosimetry, and cycling properties. See DOI: https://doi.org/10.1039/d5su00211g

into the battery. The waste and energy consumption associated with this process should be reduced to support sustainable growth within the battery industry.

Printing is a technique that could be leveraged to prepare these composite electrodes.[8] The advent and progression of movable type printing, defined as a method of printing that involves arranging separate characters or letters, has facilitated widespread access to cost-efficient books and printed materials.[9] Various printing methodologies have evolved over time, with screen printing emerging as a predominant technique on a global scale. This method consists of depositing an ink through a mesh using a squeegee. Through this basic principle, numerous variables can be manipulated to regulate the thickness of the applied film. Screen printing for electronics was first used during World War II to facilitate the mass production of electronic circuits. Screen printing was chosen to replace the manual routing of wires because it could deposit the appropriate thicknesses of the conductive material needed to carry current without excessive voltage drop. Applications were broadened to include resistors and dielectrics. This technique developed into a branch of electronic manufacturing to produce devices such as biosensors, solar cells and electronic circuits.[10–12]

In this work, screen printing techniques were used to produce composite electrodes. A bio-based sodium carboxymethylcellulose (CMC) binder was used to replace the traditional fluorinated polymers in the manufacturing process.[13] The switch is in line with recent bans on perfluoroalkyl and polyfluoroalkyl substances in many countries.[14] This was done by adapting each step of the composite electrode fabrication process to be compatible with a printable system. The physical, electrochemical and mechanical properties of the final dried composite electrodes were characterized and compared with those of conventional manufactured composite electrodes to determine how the screen printing process impacts the microstructure and hence the final properties of the electrodes. The differences in ink composition needed for compatibility with screen printing technology compared to the more conventional rod coating process were explored. Film thickness, electrical conductivity, porosity and tortuosity were evaluated. Cycling was performed in a half cell battery to examine the performance of the screen-printed and rod-coated electrode systems.[15]

2. Materials and methods

2.1 Materials

Carbon coated $LiFePO_4$ (c-LFP), type P2, was purchased from Johnson Matthey. Super C65 (carbon black) was purchased from TimCal. Sodium carboxymethylcellulose (CMC) ($M_w = 250\,000$ g mol^{-1}) was purchased from Sigma Aldrich. Carbon coated aluminum was purchased from ARMOR GROUP. The carbon-coated aluminum was pre-treated by heating it in air (220 °C for 2 h) for its use with a water-based suspension. Lithium metal laminated onto copper foil was purchased from MSE Supplies. 1 M $LiPF_6$ EC : EMC (1 : 1) electrolyte was purchased from Sigma Aldrich. A Celgard H2013 trilayer microporous membrane was used as a separator for electrochemical measurements.

2.2 Printability characterization

2.2.1 Suspension preparation. Solutions containing 4 wt% CMC in distilled water were prepared according to Table 1. The CMC was dissolved in water by stirring overnight. $LiFePO_4$ and carbon black were mixed using a mortar prior to being added to the CMC solution. The mixture was then agitated for 30 minutes using a planetary centrifugal mixer (AR250, ThinkyCorp). Different composition suspensions are studied and presented in the ESI files (Table S1†).

2.2.2 Contact angle measurements. Contact angle measurements were performed using an OCA 25 goniometer (DataPhysics) to assess the wettability between the selected substrate and the suspension containing c-LFP, C65, and CMC. Contact angle measurements (sessile drop) were performed using three different solvents: water, glycerol, and a mixture of ethylene glycol and toluene to determine the total free surface energy of the substrate using the Zisman model. Droplet behavior after stabilization was monitored for 60 s using a video camera system. Contact angle data was captured at $t = 10$ s post drop casting. Pendant drop measurements were also performed to evaluate the surface tension of the suspension. The analysis of the drop shape is based on the Young–Laplace equation (eqn (1)).

$$\Delta p = \sigma\left(\frac{1}{r_1} + \frac{1}{r_2}\right) \quad (1)$$

where Δp represents the pressure difference of the curved surfaces of the drop, r_1 and r_2 are the two radii, and σ denotes the surface tension. The recorded video/images used for contact angle and pendant drop measurements were analyzed using the DataPhysics Instrument software (dpiMAX).

2.2.3 Rheological measurements. Rheological measurements were carried out using a Discovery Hybrid H2 rheometer (TA Instruments). The rheological studies were conducted immediately after suspension preparation using a 20 mm diameter plate geometry with a 250 μm gap for each test. Flow sweep tests were performed at shear rates ranging from 0.01 s^{-1} to 1000 s^{-1} and a constant temperature of 25 °C. Thixotropy measurements were performed by measuring the suspension viscosity at different shear rates with steps of 0.1 s^{-1} to 100 s^{-1}. Each step lasted for 60 s. Amplitude sweep measurements were completed at oscillation strains between 0.1% and 1000% at an angular frequency of 10.0 rad s^{-1} over a 300 s period.

2.3 Composite electrode preparation

2.3.1 Rod coating. The suspension was coated onto a carbon-coated aluminum current collector at a rate of 25.4 mm s^{-1} using a Meyer rod (54 μm). The resulting film was

Table 1 Composition of the suspension formulations used in this study

	$LiFePO_4$ (%)	Carbon black (%)	CMC (%)	Solid content (%)
RC-CMC	89.8 ± 0.1	4.9 ± 0.2	5.2 ± 0.2	32 ± 3
SP-CMC	90.4 ± 0.1	4.5 ± 0.1	5.0 ± 0.1	36 ± 1

dried at 30 °C for 3 h, before being dried under static vacuum from 0 to −30 mmHg for 24 h.

2.3.2 Screen printing. Screen printed composite electrodes were produced using the Ekra X1SL Semi-Automatic Flat Bed Screen Printing Press. Fig. S1† illustrates the theoretical methodology and experimental setup of the flatbed screen printing process. The ink was pressed against the screen (polyester mesh with 60 monofilaments per cm), using a rubber squeegee at an angle of 45° between the screen and the carbon-coated aluminum current collector. The ink was printed at a rate of 35 mm s^{-1}. The resultant film was dried at 30 °C for 3 h, before being dried under static vacuum from 0 to −30 mmHg for 24 h.

The final composite electrodes obtained using both processes were stored under dynamic vacuum to prevent interaction with air.

2.4 Composite electrode characterization techniques

2.4.1 Mercury intrusion porosity. The tested electrodes were cut into 1 cm × 4 cm rectangular strips. The electrode was rolled in the direction of the long axis and the cylinder-shaped strip was placed in the bulb of a calibrated 5 cm^3 penetrometer (model 09 – Micromeritics). The sealed penetrometer was then introduced into the low-pressure chamber of an AutoPore V (Micromeritics) which was then put under vacuum (atmosphere to 0.20 Torr) at a rate of 2.0 psia min^{-1}. Rapid evacuation was performed down to 0.05 Torr. The penetrometer was then pumped for 5 minutes. When the penetrometer was filled with mercury (tripled distilled quality), the pressure was ≈0.01 Torr. Once filled, the pressure in the pneumatic circuit was brought to 0.5 psia (25.9 Torr) and the low-pressure analysis began. Air (99.998, bone dry, Linde) was used to force mercury into the sample. The instrument was set to record 25 points per decade between 0.5 psia and 35 psia. The system was allowed to equilibrate for 10 s after each pressure step. The intrusion rate of mercury into the sample was monitored during this time. The low-pressure method imposes an intrusion rate of ≤0.100 μL g^{-1} s^{-1} before the next pressure step was applied. The penetrometer was introduced into the high-pressure chamber of the instrument once a pressure of 35 psia was reached. Analysis was performed at pressures up to 60 000 psia using the same intrusion method as describe above. Data analysis and artefact corrections are reported in the ESI file.†

2.4.2 Scanning electron microscopy (SEM). A cross-section of the screen-printed and coated electrodes was analyzed using a scanning electron microscope (SEM, ThermoFisher Quattro). The sample was prepared from a 10 mm circular electrode encapsulated in an epoxy resin mold, which was polished (Buehler) using silicon carbide sandpaper for 2 minutes, progressively decreasing the grit size from 80 to 8 mm. To enhance conductivity, a 7 nm gold film was sputtered onto the otherwise insulating epoxy mold. The micrographs presented in the ESI† were acquired using secondary electrons at an accelerating voltage of 20 kV.

2.4.3 Electronic resistance. The electronic resistance across the thickness of the composite electrode was measured between two copper plates after subtracting the resistance of the wires. A micrometer was used to ensure that the distance between the plates was always greater than or equal to the thickness of the electrodes, allowing for a pressure similar to that in a coin-cell setup. The sheet resistance within the plane of the electrodes was also determined using a 4-point probe (Ossila). In both experiments, composite electrode discs with a diameter of 16 mm were used for measurement. The measurements were performed under ambient conditions.

2.4.4 Tortuosity factor. Tortuosity factor measurements were carried out using the technique proposed by Landesfeind *et al.*,[16,17] based on graphical fitting of electrochemical impedance spectroscopy (EIS) data. Eqn (2) describes the relationship between tortuosity and the actual ionic resistance through a cross-sectional area.

$$\tau = \frac{R_{\text{ion}} A \epsilon k}{2d} \tag{2}$$

where τ represents the tortuosity, R_{ion} the ionic resistance through the composite electrode, A is the area of the electrode, ϵ is the porosity of the electrode (determined using Hg Porosity), k is the ionic conductivity of the used electrolyte and d is the thickness of the composite electrode.

R_{ion} can be estimated using EIS under blocking conditions, meaning that no charge transfer nor faradaic reactions occur across the solid/liquid interface. This makes polarization the only observable phenomenon. Charge transfer reactions were limited using blocking conditions which involved using (1) a non-intercalating electrolyte that is electrochemically stable and (2) blocking electrodes. To achieve this, all tortuosity measurements were conducted by assembling symmetric cells (c-LFP *vs.* c-LFP system) where both composite electrodes had the exact same masses and thicknesses. Symmetric electrodes were separated using one sheet of Celgard H2013, soaked in an electrolyte made of 10 mM tetrabutylammonium perchlorate (Sigma-Aldrich). The ionic conductivity of the electrolyte was measured using a platinum conductivity cell with a cell constant of 1 (Jenway, 027815) at 25 °C. This system was assembled in a stainless-steel coin cell to maintain the same pressure applied to the electrodes so that the tortuosity measurements are representative of the galvanostatic cycling measurements.

2.4.5 Galvanostatic cycling. Galvanostatic cycling with potential limitation in half-cells (c-LFP *vs.* lithium metal) was conducted to gain a better understanding of the actual electrochemical behaviors of both the printed and cast composite electrodes. The electrodes were prepared and assembled in stainless-steel coin cells, immersed in 1 M LiPF6 EC : EMC (1 : 1) organic electrolyte, and separated by one sheet of Celgard H2013. The electrochemical performances of the cells were evaluated between 2.5 V and 4 V *vs.* Li^+/Li. All cells were cycled using a VMP potentiostat (Biologic, France) at room temperature. Each sample was tested a minimum of three times.

3. Results and discussion

A composite positive electrode for lithium-ion batteries is a complex system that undergoes various mechanisms

throughout the cycling process. That is why it is important to define the chosen system and highlight its main advantages. Fig. 1 presents the four different components presented in the studied composite electrode. Carbon coated lithium iron phosphate (c-LFP),[18–20] the electrochemically active material, is the primary component of the electrode (>80%$_{wt}$). c-LFP is widely known and commercially available. It is considered to be more sustainable than other active materials as its raw materials are both highly abundant and non-toxic. Furthermore, c-LFP is less sensitive to water than other cathode materials are.[21] This makes it suitable for processing in a water-based slurry.[22] In addition to the active material, a polymeric binder is needed to ensure the mechanical integrity of the composite electrode. This role is ensured by promoting the interconnection between the active material and carbon black at the current collector (see Fig. 1). Polyvinylidene fluoride (PVDF) is the most commonly used binder material for cathode applications due to its thermal, chemical and electrochemical stability over a large potential window. However, the use of this binder does not meet either the sustainability criteria mentioned previously or the compatibility requirements for the screen printing process. PVDF is a per- and polyfluoroalkyl substance (PFAs) and can only be dissolved in *N*-methyl-2-pyrrolidone (NMP), which is a highly toxic solvent that is both mutagenic and teratogenic.[23–26] The screen printing process involves the use of polyester mesh screens and UV-curable photoemulsions. Emulsions used in this study are incompatible with NMP, which can degrade the photoemulsion layer and compromise the printing quality.[27] CMC, which already has some established use as a binder material for Li-ion batteries, is used here as a more environmentally friendly alternative and is compatible with the screen printing parameters used.[28–30] This biobased polymer, produced by the insertion of carboxymethyl groups in natural cellulose, was first used as a thickening agent, but has been shown to produce adequate suspensions when used as a binder in electrodes. These properties are related to its electrochemical stability and its adsorption and conformation around particles that create a bridging mechanism which enables a homogeneous morphology.[31] Carbon additives such as C65 have also been added to the composite electrode to enhance its overall electronic conductivity. The composite electrode suspension is prepared by mixing these three components in water. The obtained suspension is coated onto the current collector to allow for the free flow of electrons in the battery's external circuit. In the case of screen printing processing, the printed suspension is called an ink. Carbon coated aluminum is used as a current collector because it is known to resist corrosion when used with water-based inks.[32] The current collector and specifically, the carbon coated aluminum current collector, is usually made for a specific ink's formulation and has to be compatible with the different components present in the ink.[33] The compatibility with the chosen current collector for this study and the formulated ink has also been confirmed with surface tension characterization (see section 3.2 Wettability: surface tension measurements).

The primary objective of this work is to verify the printability of the CMC-based ink during screen printing (referred to as SP-CMC). This process will entail analyzing the microstructure of the resulting electrode and correlating that microstructure with the electrochemical characteristics of the electrode. For comparison, the same system was processed using a conventional technique (Meyer rod coating, referred to as RC-CMC) with the aim of highlighting the validity and reliability of screen printing manufacturing for battery applications.

3.1 Assessing printability

Articles about functional printing of components such as electrodes have already been published in the past, demonstrating a new way of processing electrodes which can be fast, efficient and compatible with scale-up.[34–37] Fig. S2† describes the upscaling process, transitioning from a flatbed to a rotary screen printing process, that can enable roll-to-roll processing suitable for industrial-scale production.[38] This manufacturing process is described as a promising alternative to rod coating for specific energy storage applications. Yet, the development of such a process is still under development and life cycle analysis (LCA) should be considered to follow the whole sustainability process of its manufacturing. However, the feasibility of such

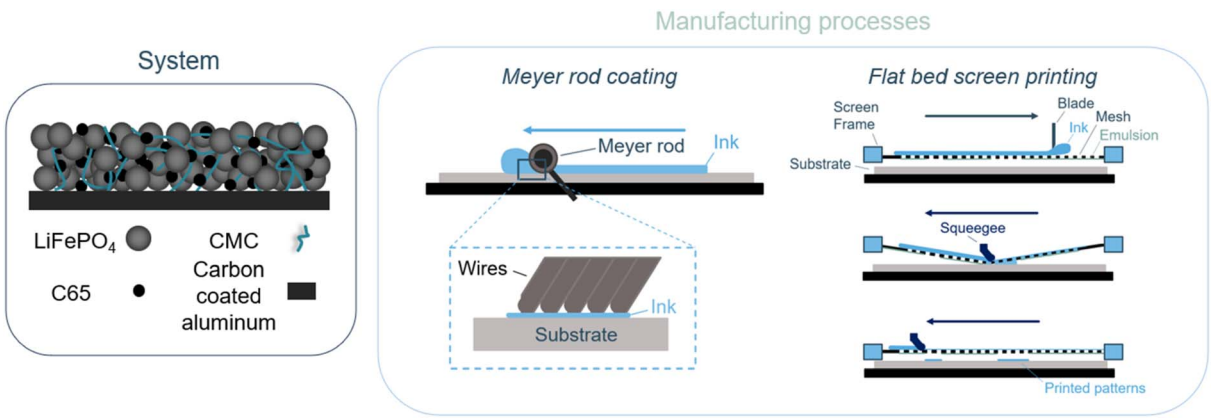

Fig. 1 Schematic representation of the electrode composition and of the manufacturing processes used in this study: Meyer rod coating (RC-CMC) and flat bed screen printing (SP-CMC).

processes for the preparation of printed batteries has received more limited attention. Several articles have explored electrode printing in Zn/MnO_2 and Li-ion battery systems. These works provided limited analysis of the printed materials and the microstructure of the printed components which are the focus of this article.[8,39,40] Alkaline printed batteries were even upscaled and commercialized for applications such as traceability. For example, Varta has demonstrated the partiality of printed battery systems adaptable to various form factors.[41] Several steps were taken to evaluate the properties of the ink and to ensure printing efficiency in terms of both fidelity and functionality. Printability can then be characterized by the quality of (1) the transfer of an ink onto a printing substrate using a printing process, (2) the capability of the ink to wet the surface, and (3) the proper contact angle and adhesion onto the substrate in liquid and dry states, respectively.[42] Fig. 2 presents how printability can be assessed using different characterization techniques.

3.2 Wettability: surface tension measurements

The wettability of the functional suspension on the chosen substrate must be characterized following printing. Contact angle analysis is an accepted method to evaluate interfacial compatibility in surface chemistry.[43] The substrate in a conventional composite electrode is the current collector. This is typically a metal foil which provides the electrons with a pathway toward the external circuit. The current collector used in this study is a carbon-coated aluminum substrate. This current collector is commonly used for the positive electrode in Li-ion batteries because its electrochemical stability reaches 3 V (*vs.* Li^+/Li) and is more electronically conductive than regular aluminum foil.[44–47] The carbon-coated aluminum substrate was thermally treated prior to use to resist corrosion due to exposure to the water-based suspension.[32] The surface energy of the substrate must be evaluated to better understand the wettability of the suspension on the surface of the substrate. Fig. 3 highlights the contact angle measurements that were performed not only to understand the affinity between the substrate and the suspension, but also to ensure that the measured values are adequate for the screen printing process.

The surface energy of the carbon coated aluminum was measured with four different solvents using the Zisman model (Fig. S3†): deionised water, ethylene glycol, glycerol and diiodomethane. The surface energy calculated for this substrate is 44.0 mN m^{-1}, corresponding to the one reported in the literature for a carbon material (45.3 mN m^{-1}).[48,49] Pendant drop tests were performed to quantify the surface tension of the suspensions that were prepared for rod coating and screen printing. For both dispersions, the surface tension was estimated to be around 30 mN m^{-1}. The surface tension values observed for both suspensions are inferior to the surface energy of the substrate: this indicates an efficient wettability between the chosen substrate and the dispersions.[50,51] In addition to these analyses, contact angle measurements were done for the components of the suspension (distilled water, 4 wt% CMC in distilled water and C65-4 wt% CMC in distilled water) (Fig. 3). This test showed how the use of different materials will impact the wettability of the suspension on the current collector. The obtained contact angles show that adding CMC and C65 to the suspension reduces the contact angle with the current collector. A droplet of deionized water shows a contact angle of 123 ± 1°. When adding CMC and C65 in water, the contact angle of the suspension decreases to 90 ± 1°. The reduction in contact angle can be explained by the higher affinity between the carbon residuals present on the current collector and carbon particles in the CMC and CMC-C65 solutions. This observation shows that the chosen materials are compatible with each other, and that they enhance the surface wettability of the current collector, making them suitable for use in the screen printing process.[52,53]

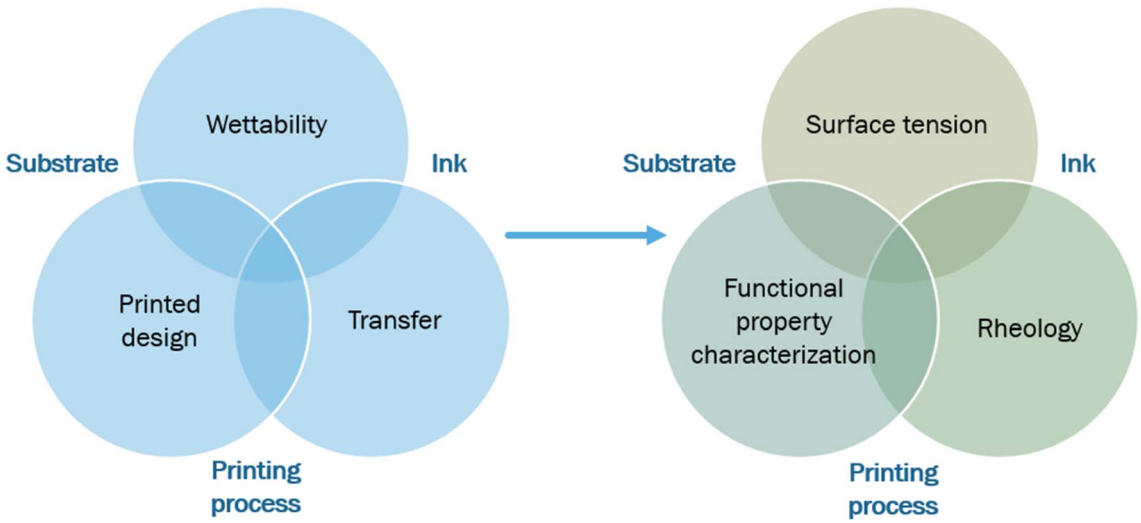

Fig. 2 Schematic representation describing the three-step assessment of printability: the wettability of the ink on the substrate that is correlated to the surface tension of the ink and the current collector; the transfer onto the substrate that can be assessed by rheological characterization; and the printed design that is characterized by its functional (chemical, mechanical and electrochemical) properties.

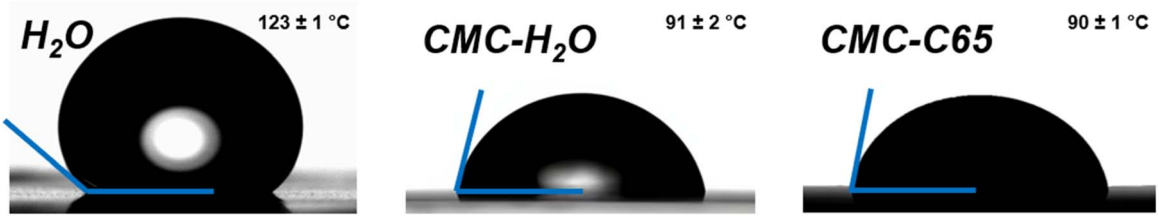

Fig. 3 Contact angle measurements for the components of the suspension on the current collector substrate: H_2O, CMC (4 wt%) solubilized in H_2O, and CMC (4 wt%) and C65 (4 wt%) solubilized in H_2O.

3.3 Transfer: rheological characterization

Rheological tests of printing inks are one of the most important steps as they simulate what is going on during the printing processes and thus indicate if the suspension is suitable for the chosen manufacturing technique.[7,54] As shown in Fig. 4, three different tests have been realized to understand and validate the rheological response of a processable suspension.[55]

Fig. 4(a) shows the results of a flow sweep test. This common rheological test is used to evaluate the shear thinning behavior of the suspensions.[56] This test, which shows the viscosity of the suspensions as a function of shear rate, allows the behavior of the suspension during manufacturing to be extrapolated. Most lithium-ion electrode suspensions exhibit shear-thinning behavior which is enhanced by the higher solid content suspensions.[57] Fig. S4† highlights the viscosity increase at very low shear rates as the particle concentration increases in the systems: 17 Pa s^{-1} for the CMC solution, 215 Pa s^{-1} for the CMC-C65 mixture and 1083 Pa s^{-1} for the cLFP-C65-CMC solution at a shear rate of 0.04 s^{-1}.

CMC as a carbohydrate plays an important role in defining the shear-thinning behavior of the suspension: its rigid

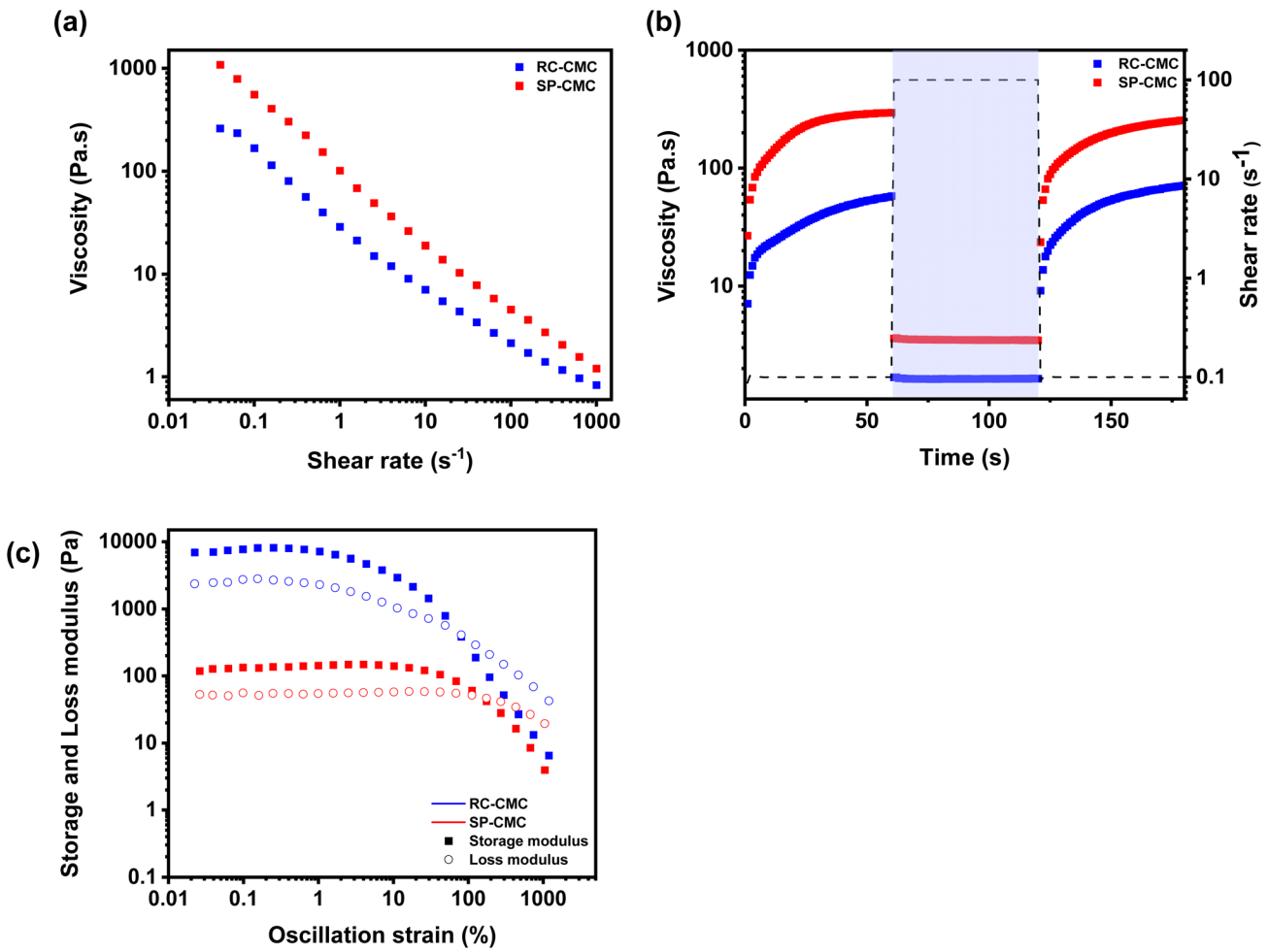

Fig. 4 Rheological characterization of RC-CMC and SP-CMC suspensions: (a) flow sweep tests: viscosity as a function of shear rate, (b) thixotropy tests, (c) storage modulus (G') and loss modulus (G'') at different applied strains during oscillatory testing.

cellulosic structure, in contrast to materials such as vinyl and acrylic, leads these polymers to adopt an extended conformation in solution, resulting in elevated viscosity levels at low shear rates. At higher shear rates during flow sweep measurements, the alignment of the polymer chains induces significant shear-thinning characteristics.[58] The non-Newtonian property of the suspensions proves to be beneficial in the electrode manufacturing process as it enables the suspension to reach an appropriate viscosity value. This targeted value can vary according to several parameters such as the mesh count of the screens or the printing rate. A low-viscosity suspension is essential for achieving adequate surface coating or printing at a high shear rate, while a higher viscosity can effectively inhibit particle sedimentation during drying.[59]

Each technique used to process the composite electrodes is correlated to a maximum shear rate which the suspension must withstand during the process. Shear rates reaching 10 000 s^{-1} can occur during screen printing when the ink penetrates the screen mesh. This is caused by the movement of the squeegee on the surface of the screen. The ideal ink for the screen printing process would exhibit low viscosity, around 1–10 Pa s, during the transfer step (*i.e.*, at a high shear rate), while exhibiting higher viscosity (a factor of 250× higher) at low shear rates (<1 s^{-1}).[60] The associated shear rate of the rod coating method is lower, around 100 s^{-1}. These shear rate requirements will thus impact how the suspension should be formulated to meet the requirements of both techniques.[61–63] Furthermore, in the case of printing, which offers freedom in the design and architectural aspects of the print, the effects of blurring and the associated lack of definition must be considered. Therefore, the ink used in flat bed screen printing will have a higher viscosity than that used for rod coating to maintain the integrity of the design and ensure sharp edges. The SP-CMC formulation was designed to fit within the acceptable viscosity range, which is from 1 to 10 Pa s for a shear rate of up to 1000–10000 s^{-1}. More precisely, at 1000 s^{-1}, the measured viscosity of the mixture is 1.20 Pa s. In comparison, the RC-CMC formulation should have a lower viscosity to align with lower shear rates of 50–100 s^{-1}.[64] The measured viscosity of the RC-CMC suspension reaches 3.21 Pa s at 100 s^{-1}.

The rheological properties of the suspension formulations were further studied using three-interval thixotropy tests (3ITT). These tests measure the rapid recovery of the suspension's elastic modulus after undergoing a large amplitude oscillatory shear. Fig. 3(b) shows the suspension response after structural deformation (100 s^{-1} during 60 s). Both suspensions exhibited the same shear-thinning behavior at the higher shear rate, despite the difference in their viscosities. The suspensions recovered their initial viscosities during the 60 s recovery period. The viscosity of the RC-CMC remained around 60 Pa s, while the viscosity of the SP-CMC ink stood at 270 Pa s. These values confirmed that the equilibrium value obtained following the application of a high shear rate is the same as the viscosity value after the first-time interval. The initial macromolecular arrangement in solution can therefore be fully recovered post microstructure disruption.[65] In the printing field, this measure can help in assessing the definition of the chosen design and to determine whether any artifacts or drips will be present in the final print.[66] Oscillation measurements provide information about the suspension behavior and stability as a function of an applied strain.

Fig. 3(c) presents the storage and loss moduli as a function of the applied oscillation strain. For the RC-CMC and SP-CMC suspensions, the storage modulus G' dominates over the loss modulus G'' in the low strain range until the flow point is reached. This corresponds to the critical strain where the viscous portion will dominate and induce the suspension to flow. The solid elastic behavior observed at lower strain corresponds to an organization that can be considered as gel-like behavior with the interaction that CMC forms when it interacts with C65 and cLFP particles.[58] Fig. S5† highlights this change in rheological behavior between CMC solutions, C65-CMC and cLFP-C65-CMC suspensions. As particle concentration in the suspension mixture rises due to C65 addition, the CMC solution transitions from behaving like a viscous liquid to behaving like an elastic solid. This phenomenon can be explained by CMC/C65 electrostatic repulsion. This results in the formation of a network that is comprised of colloidal C65 particles that are interlinked by CMC chains which cover the entirety of the system.[31] The flow point of the RC-CMC suspension is observed at a lower strain value than that of the SP-CMC suspension. This correlates with the yield point values, which are much higher for the SP-CMC suspension than for the RC-CMC suspension (Table S2†). These viscoelastic responses prove that the SP-CMC ink is stable over a larger strain range than the RC-CMC suspension. These differences make these suspensions suitable for use in their respective manufacturing techniques. Rheological measurements were also conducted to assess the reproducibility of the suspension formulation. Fig. S4† presents the flow sweep test duplicate for the tested suspensions that were printed or coated onto the current collector. This figure exhibits one of the rheology's key roles, that is ensuring the reproducibility of the formulated and homogenized suspensions for each try. The suspension formulation was reproducible: the same viscosity range and slope is observed for each duplicate. These tests are needed to provide homogeneous, well controlled and reproducible electrode suspensions for rod coating and screen printing.[54]

3.4 Composite electrode properties: microstructure and electrochemical characterizations

The dried electrodes were calendered onto the current collectors to improve adhesion between the current collector and the active material. This process reduced the total thickness of each composite electrode by 33% (Table S3†). The dried electrodes were first characterized *via* microscopy to highlight the microstructure of the composites. The cross-sectional scanning electron microscopy (SEM) micrographs for the RC-CMC and SP-CMC electrodes are presented in Fig. S7.† These images suggest a similar repartition of the active material, binder and conductive agent is achieved in both processing techniques. Further improvements concerning the cross-sectional method used can be considered to push further the understanding of the microstructure arrangement.[67,68]

Mercury intrusion porosimetry was used to estimate the overall porosity of each electrode, as well as to determine the corresponding population in each pore size range.[69] Fig. 6 shows the porosity results of the SP-CMC and RC-CMC composite electrodes. The final screen-printed composite electrodes had a higher average porosity (12.4 ± 0.5 wt%) than the rod coated electrodes (11.6 ± 0.6 wt%) (Table 2). However, these porosity values are lower than the 20–30 wt% targeted for lithium-ion battery applications.[70,71] This can be directly correlated to the CMC binder that was used to prepare the electrodes. CMC has previously been found to interact with the active material, carbon black and current collectors differently than polyvinylidene fluoride (PVDF) which is the most commonly used binder material in the fabrication of electrodes for lithium-ion batteries.[72] Thus, the polymeric binder plays an important role in the microstructure of the electrode. Fig. S8 and Table S4† confirm the porosity difference between electrodes prepared with these binders: 20 wt% for PVDF and 12 wt% for CMC, to reach the same rheological properties for both inks presented previously. When comparing both results, depending on the manufacturing technique, no significant changes are observed for the overall porosity: both values are close to each other (around 12%). Looking more closely at the pore size distribution observed for both composite electrodes, the porosity population is represented in one single distribution starting from 0.09 to 0.20 μm, and thus, for both electrodes. These measurements are consistent with previously published arrangements of active material particles within the composite electrode. The pore size distribution is concentrated in one major particle size range that is dependent on the chemical composition of the binder.[73]

Porosity results enable tests to be performed to understand the composite electrodes' tortuosity, related to the pore arrangement inside the electrode.[74] EIS measurements were conducted on symmetric cells with two identical electrodes using the Landesfeind technique, to observe the resistance associated with lithium ion diffusion in the overall composite electrode.[75] As displayed in Fig. 5(b), the Nyquist plots typically consist of three main components: a distorted semicircle at higher frequencies, a 45° linear segment at intermediate frequencies, and a steeper linear portion at lower frequencies. However, in the context of transmission line model (TLM) theory, a 45° slope without any semi-circle is predicted in the high frequency range. This deviation from the TLM model can be associated with the size or distribution of pores in the composite electrode, contact between the composite material and the current collector, and the overall thickness of the electrodes.[76,77] Despite these deviations, the TLM model can be applied to extrapolate the ionic transport resistance (R_{ion}) within the pore structure, taking into consideration the cylindrical pore approximation.[78] The ionic transport resistance (R_{ion}) within the pore structure is represented by the projection of the 45° slope onto the real axis ($R_{ion}/3$). Fig. S9† exhibits the graphical linear extrapolation to obtain R_{ion}. This parameter serves as a vital metric for assessing the rate capacity of the composite electrodes. The presence of the mid-to-high frequency range can be exclusively attributed to ionic conductivity within the porous material. This is based on the assumption that the resistance encountered by ions present in the electrolyte is at least two orders of magnitude greater than that of electrons in solid electrodes.[79]

Fig. 5(c) and Table 2 present the tortuosity values obtained for composite electrodes prepared *via* the different manufacturing techniques. The tortuosity values obtained for both processes are far from the ideal value of 1 which corresponds to the shortest path that Li^+ ions can take when traveling through the composite electrode.[15] Several processes could be responsible for the observed non-ideal tortuosity. These include the distribution of materials, as well as the intrinsic porosity and heterogeneity of the whole composite electrode which can create different pathways for ion transport.[80] The tortuosity values observed in this study are lower than those that have previously been reported for c-LFP-based systems.[81] This can be directly associated with the composite thickness and loading: tortuosity is intrinsically increased as the thickness and loading are increased. Pore rearrangements in such complex structures can be associated with the processing methods used.[82] Various models have been employed over the years to predict tortuosity values in composite electrodes. The Landesfeind model, first published in 2016 and used in this study, is based on electrochemical impedance spectroscopy to assess ionic resistance in composite electrodes.[79] Previously, the Bruggeman equation was frequently used in battery models.[83] It is based on simple diffusive transport, and the resulting tortuosity factor reported in the literature considers the Bruggeman equation for spherical particles, which can deviate from the reality of composite electrodes.

The printed and coated electrodes made in this study are significantly different from those used for industrial purposes: the resultant thickness of the electrode is much lower (≈30 μm for this study), using a bio-based polymeric binder electrode. Relating this observation to Bruggeman's earlier propositions provides a rationale for tortuosity; it indicates that with low porosity exhibiting a Gaussian distribution akin to our findings, total tortuosity increases due to ionic transport dynamics occurring within confined spaces filled with inactive constituents such as carbon black.[84] The previously described inhomogeneities in structural arrangement led to electrodes

Table 2 Electrode tortuosity estimated based on EIS measurements

Sample	Thickness (μm)	Loading (mg cm^{-2})	R_{ion} (ohm m^2)	Porosity (%)	τ_{EIS}
RC-CMC	27 ± 2	4.1 ± 0.4	0.017 ± 0.002	11.6 ± 0.6	1.6 ± 0.3
SP-CMC	29 ± 2	3.9 ± 0.4	0.021 ± 0.003	12.4 ± 0.5	1.9 ± 0.2

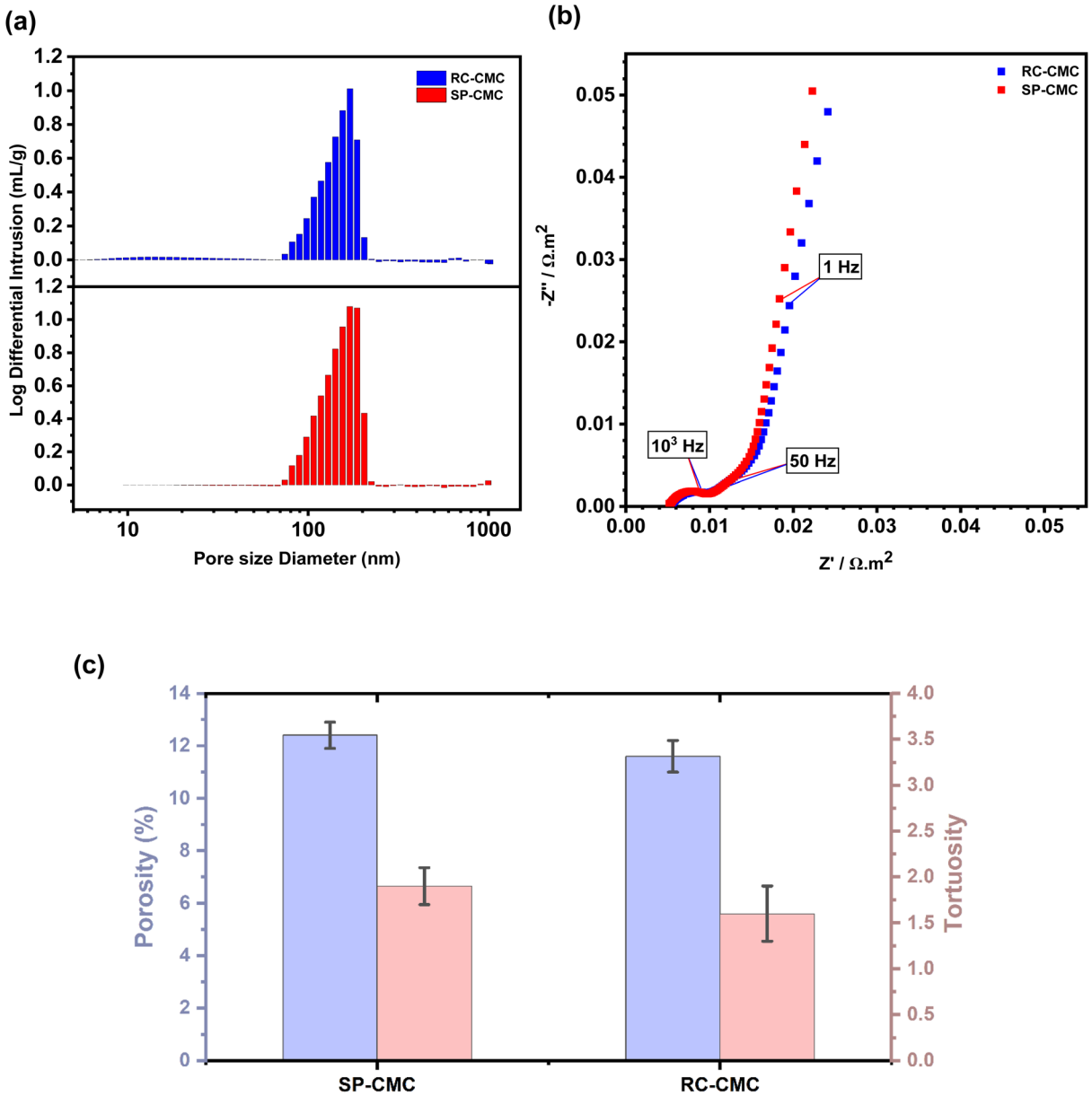

Fig. 5 (a) Pore-size distribution for RC-CMC and SP-CMC electrodes measured by mercury intrusion porosimetry. (b) Electrochemical impedance spectroscopy (EIS) spectra used for determining the tortuosity of the composite electrode. (c) Porosity and tortuosity results for the RC-CMC and SP-CMC composite electrodes.

characterized by elevated tortuosity levels, a phenomenon confirmed through our experimental methodology. Yet, the standard deviation associated with the results suggests that the obtained values are relatively close to each other. These results show that it is possible to adapt a suspension to a specialized printing process such as flat bed screen printing with a different electrode microstructure, that results in similar electrochemical properties between the two processes.

The effect of processing method on the efficiency of CMC-based c-LFP electrodes was assessed by investigating the electrochemical behavior of these electrodes using half-cell configurations (c-LFP *vs.* Li metal) with a conventional organic electrolyte (1 M $LiPF_6$ EC : EMC (2 : 1)) at different cycling rates. Fig. 6(a) shows the power performance of RC-CMC and SP-CMC electrodes charged at the same C-rates. The discharge rate was increased every 5 cycles over a range of C/10 to 1C. These measurements show that the processing method did not have a significant influence on cell performance. The intrinsic conductivity of c-LFP (both electronic and ionic) was therefore deemed to be responsible for the kinetic limitation reported at a high C-rate.[85] The increase in specific discharge capacity during the first cycles at C/20 can be ascribed to reaching a steady state, that has previously been observed for the CMC-based electrode.[22] This behavior is also in accordance with SEI (solid electrolyte interface) formation during the initial cycles which improves the overall specific capacity of the cell.[86] Similar behavior and performance were observed for SP-CMC and RC-CMC electrodes: specific discharge capacity values are

150 mA h g^{-1} at lower charging rates which is close to the theoretical capacity of c-LFP (165 mA h g^{-1}). The intrinsic conduction properties of c-LFP are responsible for kinetic limitations at higher C-rates.[85]

Fig. 6(b) exhibits the cycle life for both kinds of composite electrodes over 100 cycles at C/10. The RC-CMC and SP-CMC electrodes used in the cycling study had the same weight to facilitate comparison (RC-CMC: 0.65 ± 0.04 mA h cm^{-2} and SP-CMC: 0.67 ± 0.02 mA h cm^{-2}). The capacities of the composite electrodes were very similar over 50 cycles as is expected with similar areal coat weights. After 50 cycles, a fresh disk of lithium metal as the negative electrode was used to remove the altered lithium metal electrode.[87] Indeed, previous tests have been done using the same lithium metal electrode over 100 cycles, which resulted in capacity losses of 31% and 25% for the RC-CMC and SP-CMC composite electrodes respectively (Fig. S10†). The flat plateau (Fig. 6(b)) tilts progressively, possibly due to the contribution of lithium metal, used as a negative electrode in this system. After 50 cycles, the surface of lithium metal is altered, leading to the appearance of irregularities in the passivated interphase between lithium metal and the liquid electrolyte. However, this change in polarization occurs at the discharge state due to the use of lithium metal as a negative electrode: lithium metal stripping while discharging leads to an increase in overvoltage due to lithium metal passivation after 50 cycles. On the other hand, when charging, the plateau remains in the same place, indicating stable polarization as fresh Li metal is deposited onto the negative electrode. This hypothesis has been confirmed in Fig. 6(b). RC-CMC electrodes as well as SP-CMC electrodes exhibit similar capacities throughout the 100 cycles. Post-mortem SEM composite electrode micrographs are presented in Fig. S7,† where no drastic change was observed in the composite electrodes' microstructure and adhesion to current collectors throughout the cycles.

The electrochemical curves displayed in Fig. 6(c) and (d) reveal consistent behavior over multiple cycles at different rates for both electrodes. These are indicative of the biphasic reaction involving $LiFePO_4$ (Fe^{2+}) and FePO4 (Fe^{3+}). The data depicted in Fig. 6(a) show that the capacities of the galvanic cells that were

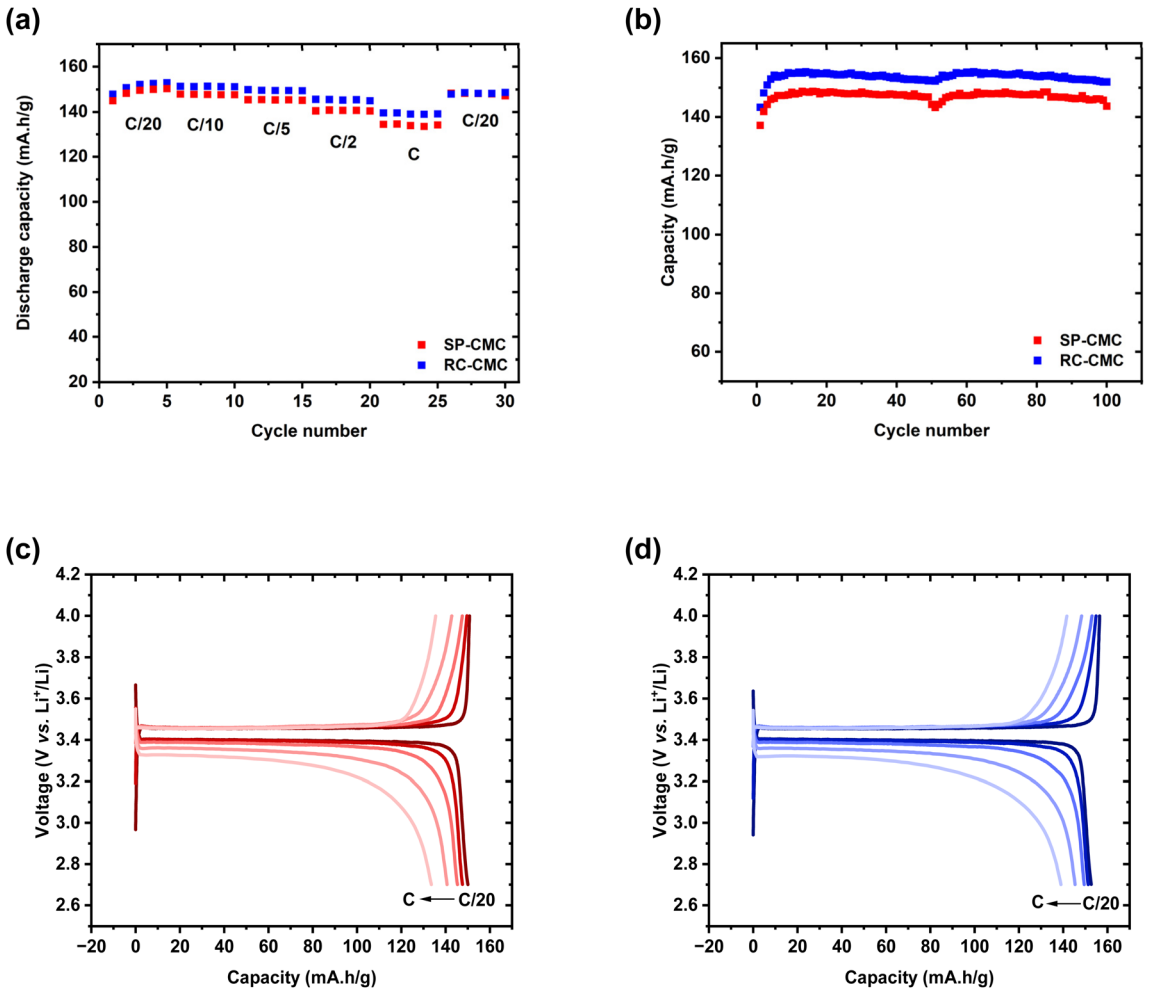

Fig. 6 (a) Ragone plot of SP-CMC and RC-CMC composite electrodes for different C-rates, (b) life cycle of the SP-CMC and RC-CMC half cells (Li metal – negative electrode with fresh lithium metal disks changed at 50th cycle) for 100 cycles, at C/10, (c) SP-CMC galvanostatic charge/discharge capacity profile of the fifth cycle at different C-rates: C/20, C/10, C/5, C/2, C, (d) RC-CMC galvanostatic charge/discharge capacity profile of the fifth cycle at different C-rates: C/20, C/10, C/5, C/2, C at room temperature.

Table 3 Voltage hysteresis at different C-rates for RC and SP-CMC electrodes at a capacity of 60 mA h g^{-1}

Sample	C/20	C/10	C/5	C/2	C
RC-CMC	0.057 mV	0.063 mV	0.081 mV	0.110 mV	0.151 mV
SP-CMC	0.056 mV	0.061 mV	0.080 mV	0.114 mV	0.156 mV

assembled with printed or cast electrodes are measured around 145 mA h g^{-1} at C/20, falling within the typical capacity range observed for c-LFP materials.[88]

The voltage hysteresis between the charge and discharge curves (Table 3) increases from 56 mV at C/20 to 151 mV at C for SP-CMC, and from 56 mV at C/20 to 156 mV at C for RC-CMC, after 5 cycles at a fixed capacity of 60 mA h g^{-1}. This is directly attributed to the increasing electrical resistance as well as the limitations of the diffusion process. This is attributed to the increasing electrical resistance as well as the limitations of the diffusion process. Li^+ ion diffusion is always associated with electron transport phenomena within the battery circuit. The internal electric field generated by the electron motion is known to strongly enhance lithium ion migration.[89]

The diffusion limitation at low rates (C/20 to C/5) is attributed to solid-state mass transport limitations within the c-LFP particles (Fig. 6(c) and (d)), while at higher rates, above 1C, the limitation is due to Li^+ transport within the electrolyte trapped in the electrode, since the amount of Li ions in the electrode alone is not enough to discharge all the FePO4 active particles.[90] The electrodes produced by screen printing with low active mass loadings show similar performance when compared to the RC-CMC electrodes. Furthermore, composite electrodes produced *via* screen printing facilitate a range of versatile applications, particularly in instances where thin composite electrodes with different architectures are required.

4. Conclusion

In summary, this study addresses challenges concerning the printability of a water-based composite electrode composed of c-$LiFePO_4$ as an active material and CMC as a bio-based polymeric binder. This approach establishes a new way to prepare composite electrodes for lithium-ion batteries. Indeed, the importance of integrating a robust approach to prepare and characterize the ink used for the printing of the electrode is discussed. The printability process is broken down into three different characterization steps which involve the assessment of the: (1) wettability by studying the surface tension and the affinity between the chosen inks and substrates, (2) ink transfer *via* functional ink rheological properties[91] and (3) properties of the printed electrodes, including porosity and tortuosity which can be used to explain the cycling and electrochemical properties of the resultant composite electrodes. The obtained results validate the adaptation of the suspension to be used to produce electrodes *via* flatbed screen printing.[92] The use of a water-based ink as well as a biobased polymer as a binder material introduces a new way of manufacturing the battery electrode system that is both more environmentally friendly and compatible with large-scale manufacturing. This article is the first step towards the introduction of a new manufacturing method to process composite electrodes for use in lithium-ion batteries. This technique can have a real impact on design freedom which can lead toward a simplified way of preparing flexible batteries for the Internet of Things.[93–95]

Data availability

The data supporting this article have been included as part of the ESI.†

Author contributions

Nora Chelfouh: conceptualization, investigation, methodology, visualization, writing – original draft and writing – review & editing. Ngoc Duc Trinh: methodology (printability: contact angle and printing process), writing – review & editing. Chloé Bois: methodology (printability: contact angle and printing process), writing – review & editing. Audrey Laventure: conceptualization, methodology (printability: rheology), supervision, writing – review & editing, investigation, project administration, funding acquisition. Mickaël Dollé: conceptualization, methodology (electrochemical properties), supervision, writing – review & editing, project administration, funding acquisition.

Conflicts of interest

The authors declare no competing financial interest.

Acknowledgements

NC thanks the Fonds de Recherche du Québec – Nature et Technologie for funding. The authors gratefully acknowledge financial support from the Canadian Foundation for Innovation, from the Natural Sciences and Engineering Research Council of Canada (NSERC), and from the Université de Montréal. AL acknowledges the Canada Research Chair program. M. D. acknowledges the Institut Courtois for the funding of his Institut Courtois research Chair. NC thanks Michel Martineau and Mike Rozel from ICI for sharing their knowledge about printing. NC acknowledges Eric Dionne from Maples for the use of mercury intrusion porosimeter systems.

References

1 G. Crabtree, Perspective: the energy-storage revolution, *Nature*, 2015, **526**(7575), S92.
2 J. T. Frith, M. J. Lacey and U. Ulissi, A non-academic perspective on the future of lithium-based batteries, *Nat. Commun.*, 2023, **14**(1), 420.
3 B. Scrosati and J. Garche, Lithium batteries: status, prospects and future, *J. Power Sources*, 2010, **195**(9), 2419–2430.
4 DESA, U., *The Sustainable Development Goals Report 2024*, UN DESA, New York, USA, 2024.
5 F. Degen, M. Winter, D. Bendig and J. Tübke, Energy consumption of current and future production of lithium-

ion and post lithium-ion battery cells, *Nat. Energy*, 2023, **8**(11), 1284–1295.
6 W. B. Hawley and J. Li, Electrode manufacturing for lithium-ion batteries—Analysis of current and next generation processing, *J. Energy Storage*, 2019, **25**, 100862.
7 P. Zhu, P. R. Slater and E. Kendrick, Insights into architecture, design and manufacture of electrodes for lithium-ion batteries, *Mater. Des.*, 2022, **223**, 111208.
8 R. E. Sousa, C. M. Costa and S. Lanceros-Méndez, Advances and Future Challenges in Printed Batteries, *ChemSusChem*, 2015, **8**(21), 3539–3555.
9 J. Mattern, *The Printing Press: an Information Revolution*, PowerKids Press, 2002.
10 C. W. Foster, R. O. Kadara, C. E. Banks, Fundamentals of Screen-Printing Electrochemical Architectures, in *Screen-Printing Electrochemical Architectures*, ed. C. E. Banks, C. W. Foster and R. O. Kadara, Springer International Publishing, 2016, pp. 13–23.
11 Y. Rong, Y. Ming, W. Ji, D. Li, A. Mei, Y. Hu and H. Han, Toward Industrial-Scale Production of Perovskite Solar Cells: Screen Printing, Slot-Die Coating, and Emerging Techniques, *J. Phys. Chem. Lett.*, 2018, **9**(10), 2707–2713.
12 D. Shukla, Y. Liu and Y. Zhu, Eco-friendly screen printing of silver nanowires for flexible and stretchable electronics, *Nanoscale*, 2023, **15**(6), 2767–2778.
13 C. G. VanGinkel and S. Gayton, The biodegradability and nontoxicity of carboxymethyl cellulose (DS 0.7) and intermediates, *Environ. Toxicol. Chem.*, 2009, **15**(3), 270–274.
14 X. Lim, Could the world go PFAS-free? Proposal to ban 'forever chemicals' fuels debate, *Nature*, 2023, **620**, 24–27.
15 R. Gonçalves, S. Lanceros-Méndez and C. M. Costa, Electrode fabrication process and its influence in lithium-ion battery performance: state of the art and future trends, *Electrochem. Commun.*, 2022, **135**, 107210.
16 J. Landesfeind, D. Pritzl and H. A. Gasteiger, An Analysis Protocol for Three-Electrode Li-Ion Battery Impedance Spectra: Part I. Analysis of a High-Voltage Positive Electrode, *J. Electrochem. Soc.*, 2017, **164**(7), A1773.
17 A. Shodiev Modeling of the manufacturing process of lithium-ion batteries : the link between electrolyte impregnation and electrochemical performance, *Modélisation du processus de fabrication des batteries lithium-ion : le lien entre l'imprégnation d'électrolyte avec électrolyte et les performances électrochimiques*, Université de Picardie Jules Verne, 2021, **https://theses.hal.science/tel-03941301**.
18 A. K. Padhi, K. S. Nanjundaswamy and J. B. Goodenough, Phospho-olivines as positive-electrode materials for rechargeable lithium batteries, *J. Electrochem. Soc.*, 1997, **144**(4), 1188.
19 N. Ravet, M. Simoneau, A. Vallée, M. Armand and J. F. Magnan, *Electrode Materials with High Surface Conductivity*, United State, 2008.
20 N. Ravet, Y. Chouinard, J. Magnan, S. Besner, M. Gauthier and M. Armand, Electroactivity of natural and synthetic triphylite, *J. Power Sources*, 2001, **97**, 503–507.
21 W. Porcher, P. Moreau, B. Lestriez, S. Jouanneau, F. Le Cras and D. Guyomard, Stability of LiFePO4 in water and consequence on the Li battery behaviour, *Ionics*, 2008, **14**(6), 583–587.
22 X. Zhang, X. Ge, Z. Shen, H. Ma, J. Wang, S. Wang, L. Liu, B. Liu, L. Liu and Y. Zhao, Green water-based binders for LiFePO4/C cathodes in Li-ion batteries: a comparative study, *New J. Chem.*, 2021, **45**(22), 9846–9855.
23 K. P. Lee, N. C. Chromey, R. Culik, J. R. Barnes and P. W. Schneider, Toxicity of N-methyl-2-pyrrolidone (NMP): teratogenic, subchronic, and two-year inhalation studies, *Fundam. Appl. Toxicol.*, 1987, **9**(2), 222–235.
24 D. E. Malek, L. A. Malley, T. W. Slone, G. S. Elliott, G. L. Kennedy, W. Mellert, K. Deckardt, C. Gembardt, B. Hildebrand, S. R. Murphy, *et al.*, Repeated Dose Toxicity Study (28 Days) in Rats and Mice with N-Methylpyrrolidone (NMP), *Drug Chem. Toxicol.*, 1997, **20**(1–2), 63–77.
25 A. Rensmo, E. K. Savvidou, I. T. Cousins, X. Hu, S. Schellenberger and J. P. Benskin, Lithium-ion battery recycling: a source of per- and polyfluoroalkyl substances (PFAS) to the environment?, *Environ. Sci. Processes Impacts*, 2023, **25**(6), 1015–1030.
26 J. L. Guelfo, P. L. Ferguson, J. Beck, M. Chernick, A. Doria-Manzur, P. W. Faught, T. Flug, E. P. Gray, N. Jayasundara, D. R. U. Knappe, *et al.*, Lithium-ion battery components are at the nexus of sustainable energy and environmental release of per- and polyfluoroalkyl substances, *Nat. Commun.*, 2024, **15**(1), 5548.
27 K. Yamaguchi, K. Igarashi, H. Tabata and H. Suzuki, Screen Printing Grade Polyimide Paste for Alpha-Particle Protection, *IEEE Trans. Compon., Hybrids, Manuf. Technol.*, 1986, **9**(4), 370–373.
28 A. Guerfi, M. Kaneko, M. Petitclerc, M. Mori and K. Zaghib, LiFePO4 water-soluble binder electrode for Li-ion batteries, *J. Power Sources*, 2007, **163**(2), 1047–1052.
29 J.-H. Lee, J.-S. Kim, Y. C. Kim, D. S. Zang, Y.-M. Choi, W. I. Park and U. Paik, Effect of carboxymethyl cellulose on aqueous processing of LiFePO4 cathodes and their electrochemical performance, *Electrochem. Solid-State Lett.*, 2008, **11**(10), A175.
30 R. Gordon, R. Orias and N. Willenbacher, Effect of carboxymethyl cellulose on the flow behavior of lithium-ion battery anode slurries and the electrical as well as mechanical properties of corresponding dry layers, *J. Mater. Sci.*, 2020, **55**(33), 15867–15881.
31 W. Porcher, B. Lestriez, S. Jouanneau and D. Guyomard, Design of aqueous processed thick LiFePO4 composite electrodes for high-energy lithium battery, *J. Electrochem. Soc.*, 2008, **156**(3), A133.
32 I. Doberdò, N. Löffler, N. Laszczynski, D. Cericola, N. Penazzi, S. Bodoardo, G.-T. Kim and S. Passerini, Enabling aqueous binders for lithium battery cathodes – carbon coating of aluminum current collector, *J. Power Sources*, 2014, **248**, 1000–1006.
33 C. Bizot, M.-A. Blin, P. Guichard, P. Soudan, J. Gaubicher and P. Poizot, Aluminum current collector for high voltage Li-ion battery. Part II: benefit of the En' Safe® primed current collector technology, *Electrochem. Commun.*, 2021, **126**.

34 P. Yang, J. Li, S. W. Lee and H. J. Fan, Printed Zinc Paper Batteries, *Adv. Sci.*, 2022, **9**(2), 2103894.
35 K. K. R. Reddygunta, L. Siller and A. Ivaturi, Screen-Printed Stretchable Supercapacitors Based on Tin Sulfide-Decorated Face-Mask-Derived Activated Carbon Electrodes with High Areal Energy Density, *ACS Appl. Energy Mater.*, 2024, **7**(9), 3558–3576.
36 A. García-Miranda Ferrari, S. J. Rowley-Neale and C. E. Banks, Screen-printed electrodes: transitioning the laboratory in-to-the field, *Talanta Open*, 2021, **3**.
37 R. Søndergaard, M. Hösel, D. Angmo, T. T. Larsen-Olsen and F. C. Krebs, Roll-to-roll fabrication of polymer solar cells, *Mater. Today*, 2012, **15**(1), 36–49.
38 M. Hösel, H. F. Dam and F. C. Krebs, Development of Lab-to-Fab Production Equipment Across Several Length Scales for Printed Energy Technologies, Including Solar Cells, *Energy Technol.*, 2015, **3**(4), 293–304.
39 Z. Wang, R. Winslow, D. Madan, P. K. Wright, J. W. Evans, M. Keif and X. Rong, Development of MnO2 cathode inks for flexographically printed rechargeable zinc-based battery, *J. Power Sources*, 2014, **268**, 246–254.
40 M.-S. Park, S.-H. Hyun and S.-C. Nam, Mechanical and electrical properties of a LiCoO2 cathode prepared by screen-printing for a lithium-ion micro-battery, *Electrochim. Acta*, 2007, **52**(28), 7895–7902.
41 VARTA AG, *Printed Batteries*, **https://www.varta-ag.com/en/industry/printed-batteries**, accessed 2025 May 13.
42 K. Sakuma, *Flexible, Wearable, and Stretchable Electronics*, CRC Press, 2020.
43 M. Abubaker, C.-H. Sohn and H. M. Ali, Understanding wetting behavior in electrode–electrolyte interface formation and its sensitivity to electrode-current collector interaction: a lattice Boltzmann method approach, *J. Therm. Anal. Calorim.*, 2024, **149**(11), 5443–5456.
44 Y. Li, X.-W. Zhang, S. A. Khan and P. S. Fedkiw, Attenuation of Aluminum Current Collector Corrosion in LiTFSI Electrolytes Using Fumed Silica Nanoparticles, *Electrochem. Solid-State Lett.*, 2004, **7**(8), A228.
45 M. Morita, T. Shibata, N. Yoshimoto and M. Ishikawa, Anodic behavior of aluminum current collector in LiTFSI solutions with different solvent compositions, *J. Power Sources*, 2003, **119–121**, 784–788.
46 T. Li, H. Bo, H. Cao, Y. Lai and Y. Liu, Carbon-coated Aluminum Foil as Current Collector for Improving the Performance of Lithium Sulfur Batteries, *Int. J. Electrochem. Sci.*, 2017, **12**(4), 3099–3108.
47 S.-K. Chen, K.-F. Chiu, S.-H. Su, S.-H. Liu, K. H. Hou, H.-J. Leu and C.-C. Hsiao, Low contact resistance carbon thin film modified current collectors for lithium Ion batteries, *Thin Solid Films*, 2014, **572**, 56–60.
48 H. Li, L. Wang, Y. Song, Z. Zhang, H. Zhang, A. Du and X. He, Significance of Current Collectors for High Performance Conventional Lithium-Ion Batteries: A Review, *Adv. Funct. Mater.*, 2023, **33**(49).
49 S. Nuriel, L. Liu, A. H. Barber and H. D. Wagner, Direct measurement of multiwall nanotube surface tension, *Chem. Phys. Lett.*, 2005, **404**(4–6), 263–266.
50 J. Li, C. Rulison, J. Kiggans, C. Daniel and D. L. Wood, Superior Performance of LiFePO4Aqueous Dispersions via Corona Treatment and Surface Energy Optimization, *J. Electrochem. Soc.*, 2012, **159**(8), A1152–A1157.
51 K.-Y. Law and H. Zhao, Determination of Solid Surface Tension by Contact Angle, in *Surface Wetting: Characterization, Contact Angle, and Fundamentals*, ed. K.-Y. Law and H. Zhao, Springer International Publishing, 2016, pp. 135–148.
52 M. Grüßer, D. G. Waugh, J. Lawrence, N. Langer and D. Scholz, On the Droplet Size and Application of Wettability Analysis for the Development of Ink and Printing Substrates, *Langmuir*, 2019, **35**(38), 12356–12365.
53 C. Lamiel, I. Hussain, X. Ma and K. Zhang, Properties, functions, and challenges: current collectors, *Mater. Today Chem.*, 2022, **26**.
54 C. D. Reynolds, S. D. Hare, P. R. Slater, M. J. H. Simmons and E. Kendrick, Rheology and Structure of Lithium-Ion Battery Electrode Slurries, *Energy Technol.*, 2022, **10**(10).
55 S. Tagliaferri, A. Panagiotopoulos and C. Mattevi, Direct ink writing of energy materials, *Mater. Adv.*, 2021, **2**(2), 540–563.
56 C. D. Reynolds, J. Lam, L. Yang and E. Kendrick, Extensional rheology of battery electrode slurries with water-based binders, *Mater. Des.*, 2022, 222.
57 J. J. Stickel and R. L. Powell, Fluid Mechanics and Rheology of Dense Suspensions, *Annu. Rev. Fluid Mech.*, 2005, **37**(1), 129–149.
58 B. Lestriez, Functions of polymers in composite electrodes of lithium ion batteries, *C. R. Chim.*, 2010, **13**(11), 1341–1350.
59 G.-W. Lee, J. H. Ryu, W. Han, K. H. Ahn and S. M. Oh, Effect of slurry preparation process on electrochemical performances of LiCoO2 composite electrode, *J. Power Sources*, 2010, **195**(18), 6049–6054.
60 S. Abbott, *How to be a great screen printer; MacDermid Autotype*.
61 H.-W. Lin, C.-P. Chang, W.-H. Hwu and M.-D. Ger, The rheological behaviors of screen-printing pastes, *J. Mater. Process. Technol.*, 2008, **197**(1–3), 284–291.
62 W. Bauer and D. Nötzel, Rheological properties and stability of NMP based cathode slurries for lithium ion batteries, *Ceram. Int.*, 2014, **40**(3), 4591–4598.
63 N. Aguiló-Aguayo, D. Hubmann, F. U. Khan, S. Arzbacher and T. Bechtold, Water-based slurries for high-energy LiFePO4 batteries using embroidered current collectors, *Sci. Rep.*, 2020, **10**(1), 5565.
64 F. A. ÇEtinel and W. Bauer, Processing of water-based LiNi1/3Mn1/3Co1/3O2 pastes for manufacturing lithium ion battery cathodes, *Bull. Mater. Sci.*, 2014, **37**(7), 1685–1690.
65 N. D. Polychronopoulos and A. Brouzgou, Direct Ink Writing for Electrochemical Device Fabrication: A Review of 3D-Printed Electrodes and Ink Rheology, *Catalysts*, 2024, **14**(2).
66 K. J. Mysels, Visual Art: The Role of Capillarity and Rheological Properties in Painting, *Leonardo*, 1981, **14**(1), 22–27.
67 J. Scharf, M. Chouchane, D. P. Finegan, B. Lu, C. Redquest, M.-c. Kim, W. Yao, A. A. Franco, D. Gostovic, Z. Liu, *et al.*, Bridging nano- and microscale X-ray tomography for

battery research by leveraging artificial intelligence, *Nat. Nanotechnol.*, 2022, **17**(5), 446–459.
68 R. Elango, A. Nadeina, F. Cadiou, V. De Andrade, A. Demortière, M. Morcrette and V. Seznec, Impact of electrode porosity architecture on electrochemical performances of 1 mm-thick LiFePO4 binder-free Li-ion electrodes fabricated by Spark Plasma Sintering, *J. Power Sources*, 2021, **488**, 229402.
69 L. Froboese, P. Titscher, B. Westphal, W. Haselrieder and A. Kwade, Mercury intrusion for ion- and conversion-based battery electrodes – structure and diffusion coefficient determination, *Mater. Charact.*, 2017, **133**, 102–111.
70 B. Lestriez, W. Porcher and T. Devic, La formulation des électrodes composites des batteries Li-ion: un enjeu technologique majeur, *Actual. Chim.*, 2021, **464**, 36.
71 J. Chong, S. Xun, H. Zheng, X. Song, G. Liu, P. Ridgway, J. Q. Wang and V. S. Battaglia, A comparative study of polyacrylic acid and poly(vinylidene difluoride) binders for spherical natural graphite/LiFePO4 electrodes and cells, *J. Power Sources*, 2011, **196**(18), 7707–7714.
72 S. Albers, J. Timmermann, T. Brake, A. Arifiadi, A. L. Gerlitz, M. Börner, M. Winter and J. Kasnatscheew, Enabling Aqueous Processing of Ni-Rich Layered Oxide Cathodes via Systematic Modification of Biopolymer (Polysaccharide)-Based Binders, *Adv. Energy Sustain. Res.*, 2024.
73 T. Beuse, M. Fingerle, C. Wagner, M. Winter and M. Börner, Comprehensive Insights into the Porosity of Lithium-Ion Battery Electrodes: A Comparative Study on Positive Electrodes Based on LiNi0.6Mn0.2Co0.2O2 (NMC622), *Batteries*, 2021, **7**(4).
74 D. Zapata Dominguez, J. Xu, Y. Boudjema, S. Ben Hadj Ali, F. M. Zanotto and A. A. Franco, Influence of the mixing speed in the rheology of NMC622-based Li-ion battery electrode slurries, *J. Power Sources Adv.*, 2024, **26**, 100141.
75 A. Shodiev, E. N. Primo, M. Chouchane, T. Lombardo, A. C. Ngandjong, A. Rucci and A. A. Franco, 4D-resolved physical model for Electrochemical Impedance Spectroscopy of Li(Ni1-x-yMnxCoy)O2-based cathodes in symmetric cells: consequences in tortuosity calculations, *J. Power Sources*, 2020, **454**, 227871.
76 M. Gaberscek, J. Moskon, B. Erjavec, R. Dominko and J. Jamnik, The Importance of Interphase Contacts in Li Ion Electrodes: The Meaning of the High-Frequency Impedance Arc, *Electrochem. Solid-State Lett.*, 2008, **11**(10), A170.
77 R. Kant and M. B. Singh, Theory of the Electrochemical Impedance of Mesostructured Electrodes Embedded with Heterogeneous Micropores, *J. Phys. Chem. C*, 2017, **121**(13), 7164–7174.
78 H. Alharbi, M. Khalid and M. Abido, Transmission Lines Impedance Fitting Using Analytical Impedance Equation and Frequency Response Analysis, *Mathematics*, 2022, **10**(15), 2677.
79 J. Landesfeind, J. Hattendorff, A. Ehrl, W. A. Wall and H. A. Gasteiger, Tortuosity Determination of Battery Electrodes and Separators by Impedance Spectroscopy, *J. Electrochem. Soc.*, 2016, **163**(7), A1373.
80 N. A. Zacharias, D. R. Nevers, C. Skelton, K. Knackstedt, D. E. Stephenson and D. R. Wheeler, Direct Measurements of Effective Ionic Transport in Porous Li-Ion Electrodes, *J. Electrochem. Soc.*, 2013, **160**(2), A306.
81 L. Yang, D. Gastol and E. Kendrick, Design principles for LiFePO4 electrodes with improved recyclability, *Green Chem.*, 2023, **25**(23), 9959–9968.
82 Y. Orikasa, Y. Gogyo, H. Yamashige, M. Katayama, K. Chen, T. Mori, K. Yamamoto, T. Masese, Y. Inada, T. Ohta, *et al.*, Ionic Conduction in Lithium Ion Battery Composite Electrode Governs Cross-sectional Reaction Distribution, *Sci. Rep.*, 2016, **6**, 26382.
83 M. Ebner and V. Wood, Tool for Tortuosity Estimation in Lithium Ion Battery Porous Electrodes, *J. Electrochem. Soc.*, 2015, **162**(2), A3064–A3070.
84 D.-W. Chung, M. Ebner, D. R. Ely, V. Wood and R. Edwin García, Validity of the Bruggeman relation for porous electrodes, *Model. Simulat. Mater. Sci. Eng.*, 2013, **21**(7).
85 W.-J. Zhang, Structure and performance of LiFePO4 cathode materials: a review, *J. Power Sources*, 2011, **196**(6), 2962–2970.
86 L. von Kolzenberg, A. Latz and B. Horstmann, Solid-Electrolyte Interphase During Battery Cycling: Theory of Growth Regimes, *ChemSusChem*, 2020, **13**(15), 3901–3910.
87 S. Li, M. Jiang, Y. Xie, H. Xu, J. Jia and J. Li, Developing High-Performance Lithium Metal Anode in Liquid Electrolytes: Challenges and Progress, *Adv. Mater.*, 2018, **30**(17), e1706375.
88 T. Bibienne, L. Maillaud, S. Rousselot, L. W. Taylor, M. Pasquali and M. Dollé, Eco-friendly process toward collector- and binder-free, high-energy density electrodes for lithium-ion batteries, *J. Solid State Electrochem.*, 2017, **21**(5), 1407–1416.
89 C. Wang and J. Hong, Ionic/electronic conducting characteristics of LiFePO4 cathode materials: the determining factors for high rate performance, *Electrochem. Solid State Lett.*, 2007, **10**(3), A65.
90 I. V. Thorat, T. Joshi, K. Zaghib, J. N. Harb and D. R. Wheeler, Understanding Rate-Limiting Mechanisms in LiFePO4 Cathodes for Li-Ion Batteries, *J. Electrochem. Soc.*, 2011, **158**(11).
91 Y. Zhang, Y. Zhu, S. Zheng, L. Zhang, X. Shi, J. He, X. Chou and Z.-S. Wu, Ink formulation, scalable applications and challenging perspectives of screen printing for emerging printed microelectronics, *J. Energy Chem.*, 2021, **63**, 498–513.
92 O. El Baradai, D. Beneventi, F. Alloin, Y. Bultel and D. Chaussy, Use of Cellulose Nanofibers as an Electrode Binder for Lithium Ion Battery Screen Printing on a Paper Separator, *Nanomaterials*, 2018, **8**(12), 982.
93 A. M. Gaikwad, A. C. Arias and D. A. Steingart, Recent Progress on Printed Flexible Batteries: Mechanical Challenges, Printing Technologies, and Future Prospects, *Energy Technol.*, 2015, **3**(4), 305–328.
94 Z. Lyu, G. J. H. Lim, J. J. Koh, Y. Li, Y. Ma, J. Ding, J. Wang, Z. Hu, J. Wang, W. Chen, *et al.*, Design and Manufacture of 3D-Printed Batteries, *Joule*, 2021, **5**(1), 89–114.
95 B. Clement, M. Lyu, E. Sandeep Kulkarni, T. Lin, Y. Hu, V. Lockett, C. Greig and L. Wang, Recent Advances in Printed Thin-Film Batteries, *Engineering*, 2022, **13**, 238–261.